Lateral association and elongation of vimentin intermediate filament proteins: A time-resolved light-scattering study

Carlos G. Lopez[a,1], Oliva Saldanha[b,1], Klaus Huber[a,2], and Sarah Köster[b,2]

[a]Department Chemie, Universität Paderborn, 33098 Paderborn, Germany; and [b]Institut für Röntgenphysik, Georg-August-Universitat Göttingen, 37077 Göttingen, Germany

Edited by David A. Weitz, Harvard University, Cambridge, MA, and approved August 11, 2016 (received for review April 21, 2016)

Vimentin intermediate filaments (IFs) are part of a family of proteins that constitute one of the three filament systems in the cytoskeleton, a major contributor to cell mechanics. One property that distinguishes IFs from the other cytoskeletal filament types, actin filaments and microtubules, is their highly hierarchical assembly pathway, where a lateral association step is followed by elongation. Here we present an innovative technique to follow the elongation reaction in solution and in situ by time-resolved static and dynamic light scattering, thereby precisely capturing the relevant time and length scales of seconds to minutes and 60–600 nm, respectively. We apply a quantitative model to our data and succeed in consistently describing the entire set of data, including particle mass, radius of gyration, and hydrodynamic radius during longitudinal association.

cytoskeleton | intermediate filaments | vimentin | self-assembly | time-resolved light scattering

Intermediate filaments (IFs) constitute one of the three protein filament systems in the cytoskeleton of metazoa. Together with actin filaments and microtubules they form a sophisticated composite network, which has been identified as a main player in cell mechanics (1). By contrast to actin filaments and microtubules, which are conserved across cell types and organisms, IFs comprise a large family of proteins, encoded by 70 genes in humans (2), and they are expressed in a cell-type–specific manner. Vimentin is an IF protein expressed in fibroblasts, the eye lens, and cells of mesenchymal origin. The monomers with a molecular weight M_w of 53.5×10^3 g/mol share their tripartite structure consisting of an α-helical rod flanked by intrinsically disordered "head" and "tail" domains, as shown in Fig. 1*A*, with all other IFs. These monomers are stable in denaturing conditions, such as 8 M urea, and assemble into coiled-coil dimers and subsequently into antiparallel tetramers with $M_w = 214 \times 10^3$ g/mol, a length of 60 nm, and a diameter of 5 nm upon stepwise dialysis into low-salt buffers, such as 2 mM sodium phosphate (3). Thus, in buffer conditions without urea, these tetramers with a mass per unit length M_L^{tet} of 3,570 g/(mol·nm) are the smallest subunits and starting precursors for vimentin IF assembly. In vitro the assembly of tetramers into full-length filaments can be initiated by the addition of, e.g., monovalent salts such as potassium chloride (KCl) at concentrations of a few tens of millimolars. It has been shown by time-lapse electron microscopy (4) and more recently by real-time small-angle X-ray scattering (SAXS) in combination with microfluidic techniques (5–7) that a lateral assembly step into unit-length filaments (ULFs) consisting of typically eight tetramers (Fig. 1*B*) is followed by an elongation reaction where ULFs and short filaments join to form micrometer-long filaments (Fig. 1*C*). However, the exact molecular mechanism of the elongation reaction remains elusive. It is clear that the tail domains are not needed (4). The way that the IF consensus domains at either end of the rod interact, overlapping (8) vs. interdigitating (9), is not clear. Moreover, the extent to which the subdomain flexibility plays a role is still uncertain (10). Importantly, the number of monomers per cross-section may vary, depending on the overall and local buffer conditions (4). Note that in the fully assembled filament, the mass per unit length is 40×10^3 g/(mol·nm), when assuming a typical number of eight tetramers per cross-section, due to a partial overlap of the ULFs during the elongation reaction.

A ULF is 60 nm long and 17 nm in diameter, and thus SAXS is a highly suitable technique to observe the lateral assembly from tetramers to ULFs (5, 11). Recently fluorescence labeling techniques have been developed for vimentin IFs (12, 13), enabling us to observe the elongational growth of filaments 1 μm long or longer. However, the length scales between ∼100 nm and 500 nm are not easily accessible by SAXS or by visible light microscopy and dynamic data of the assembly process in this range are largely missing. We bridge this gap by applying a combination of time-resolved static light scattering (SLS) and dynamic light scattering (DLS), which accesses exactly the missing length scales and is sensitive in the range of contour lengths between 60 nm and 600 nm.

SLS is a very suitable technique to determine the mass and structure of protein aggregates and assemblies in dilute solution with radii of gyration and molar masses in the range of 10–200 nm and 5×10^3–1×10^8 g/mol, respectively. DLS further allows us to measure the distribution of relaxation times in solution (14, 15), from which diffusion coefficients can be extracted. An early study of aggregation applying combined SLS and DLS analyzed the initial stage of coagulation of spherical colloids (16). Time-resolved SLS was used to record the consumption of triarylamine

Significance

The hierarchical assembly pathway of the cytoskeletal protein vimentin may be responsible for the astonishing mechanical properties of the emerging filaments, such as high flexibility and extensibility, and thus play a key role in cellular mechanics. A two-step assembly mechanism, involving a lateral and a subsequent elongational step, has been established; however, the elongational step could not be followed in solution. Here, we show direct in situ observation and modeling of the elongation reaction of the filaments on the relevant length and time scales, using time-resolved, multiangle static and dynamic light scattering. We thus achieve sufficient spatio-temporal resolution without the need of labeling, staining, or adsorption to substrates.

Author contributions: K.H. and S.K. designed research; C.G.L. and O.S. performed research; C.G.L. analyzed data; C.G.L., O.S., K.H., and S.K. wrote the paper; C.G.L. performed theoretical calculations; O.S. prepared protein samples; K.H. interpreted data and performed theoretical calculations; and S.K. interpreted results.

The authors declare no conflict of interest.

This article is a PNAS Direct Submission.

[1]C.G.L. and O.S. contributed equally to this work.

[2]To whom correspondence may be addressed. Email: klaus.huber@upb.de or sarah.koester@phys.uni-goettingen.de.

This article contains supporting information online at www.pnas.org/lookup/suppl/doi:10.1073/pnas.1606372113/-/DCSupplemental.

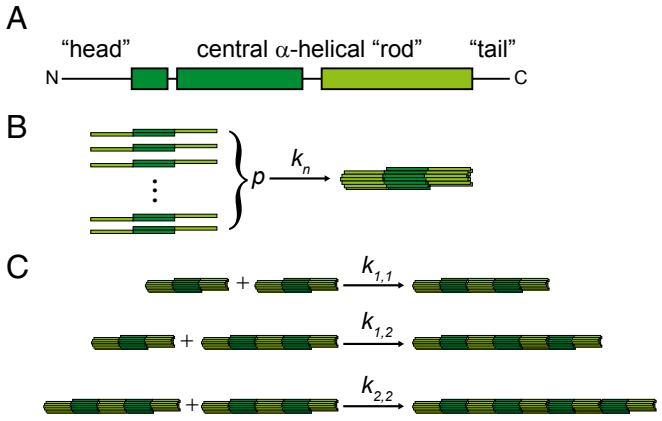

Fig. 1. (*A*) Vimentin monomer structure with the central α-helical rod domain (green boxes; light and dark green for facilitating understanding of the assembly hierarchy) and intrinsically unstructured head and tail domains (black lines). Monomers form antiparallel tetramers, consisting of two coiled-coil dimers, in low-salt buffers. (*B*) Lateral assembly step. *p* tetramers associate to form a ULF. (*C*) Elongation reaction. Association of ULFs or filaments of any length are included in our model.

molecules during their self-assembly and supplementary DLS succeeded in attributing a decreasing scattering signal to the monomers and nuclei disappearing during assembly (17). SLS and DLS have also been applied to study fibril formation in amyloid-β in the time range of a few seconds to days (18–22). In the case of fast kinetics, experiments had to be restricted to single-angle recordings due to the moderate temporal resolution of the methods. The limitations of single-angle DLS or SLS/DLS setups imply that to interpret kinetic data, specific assumptions have to be made about the morphology of aggregates. As an example, Lomakin et al. (19) and Pallitto and Murphy (23) in their studies of amyloid-β fibers had to assume a cylinder-like (24–26) structure of their aggregates and to use model-based equations and simplifications to extrapolate data to a state suitable for a kinetic analysis.

Our work extends the technique to a multiangle setup enabling time-resolved combined SLS and DLS. Compared with single-angle setups, where assumptions about the morphology and size distribution of the particles are necessary to extract structural parameters, multiangle light scattering permits reliable extraction of the molecular weight (M_w), radius of gyration (R_g), and hydrodynamic radius (R_H) without specific assumptions about the shape and the degree of polydispersity of the particles, as previously demonstrated for the aggregation of dyestuff molecules and for nucleation and growth of silica particles (27, 28). Application of this in situ technique provides us with a consistent set of M_w, R_g, and R_H of assembling filaments and enables us to follow quantitatively and in real time the longitudinal growth of ULFs toward filaments of lengths up to 600 nm. The resulting data are compared with a kinetic model of a step growth process (23).

Theoretical Background

SLS from a dilute solution of weakly interacting particles can be approximated by (24)

$$\frac{Kc}{R_\theta}=\frac{1}{P(q)M_w}+2A_2c\simeq\frac{1}{M_w}\left(1+\frac{q^2\langle R_g^2\rangle_z}{3}\right)+2A_2c. \qquad [1]$$

DLS measures the intensity correlation function $g_2(t)$ from which the inverse relaxation time Γ can be obtained. Γ depends on the scattering vector in the low q limit as

$$\Gamma/q^2=D_z\left(1+q^2\left\langle R_g^2\right\rangle_z C+k_Dc\right). \qquad [2]$$

D_z is the z-averaged diffusion coefficient and C and k_D describe the angle and concentration dependence of Γ, respectively. D_z for cylinders can be calculated according to Eq. **S10**. The Stokes–Einstein equation translates the diffusion coefficient into an effective hydrodynamic radius:

$$R_H=\frac{k_BT}{6\pi\eta D_z}. \qquad [3]$$

The parameter R_H is defined as the radius of a sphere exhibiting the same diffusion coefficient as the particles under current consideration. R_H differs from R_g, which is a purely geometric quantity. The actual difference depends on the particle shape and can be quantified by the ratio $\rho=R_g/R_H$ (29).

Results and Discussion

Characterization of Vimentin Before Initiation of Assembly. SLS and DLS measurements of nonassembled vimentin in dilute solution before the addition of KCl show different values of M_w, R_g, and R_H for samples with slightly varying sample histories (e.g., different stock solutions, dialysis, and filtering in different batches) as shown in Fig. 2 (see also Tables S1 and S2). The values for M_w and R_g are always larger than those of a tetramer with M_w = 214 kg/mol, $R_g \simeq 17$ nm ($R_g \simeq L/\sqrt{12}$ for rods). The polydispersity (*p.d.*), expressed as the ratio of the weight-averaged molecular weight M_w and number-averaged molecular weight M_n (see *Supporting Information*, *Application of the Rod Model to Light Scattering* for the mathematical definitions), is found to vary between 1.3 and 2.2, with higher-M_w samples generally showing higher *p.d.* This result suggests that species larger than tetramers are present in our starting solutions.

To evaluate the parameters A_2 and k_D (Eqs. **1** and **2**) and to scrutinize whether dilution affects the aggregation in the

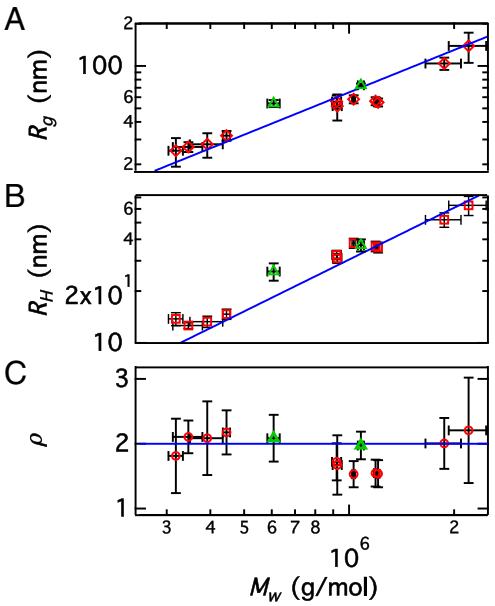

Fig. 2. Aggregation of unassembled vimentin. (*A*) Square root of the z-averaged squared radius of gyration R_g plotted against weight-averaged molar mass M_w. The blue line indicates a power law with exponent 1. (*B*) Hydrodynamic radius R_H plotted against M_w. The blue line indicates a power law with exponent 1. (*C*) Shape-sensitive ratio $\rho=R_g/R_H$ plotted against M_w. The blue line indicates the average value of $\rho=2$. The values extrapolated to infinite dilution from Zimm plots are included as green triangles (*Supporting Information*, *Zimm Plots of Dilution Series of Vimentin in Sodium Phosphate Buffer*).

PHYSICS

concentration regime under consideration, two samples were stepwise diluted and remeasured and M_w, R_g, and R_H were extrapolated to $c = 0$ and included in Fig. 2 as green triangles; they agree well with the general trend. The results are plotted in Fig. S2 and A_2 and k_D are given in Table S2. Thus, a concentration-dependent variation of the aggregation can be excluded as the cause of the observed sample characteristics. The absence of a correlation between the parameters shown in Fig. 2 and their corresponding concentrations (Tables S1 and S2) further supports insensitivity of the aggregation state to the protein concentration in the range studied.

The effect of filtering, which is capable of breaking assemblies to some degree, is discussed in *Supporting Information*, *Effect of Filtering* and may be a potential cause of the variation observed within the present set of samples. Two different scenarios for our starting solution are consistent with the data shown in Fig. 2. First, it is possible that each individual sample represents a homogeneous population of rods at different lengths and masses, thus leading to the three distinct "groups" of data visible in Fig. 2. The constant value of ρ within experimental error suggests self-similarity in the structure of different samples (29). Both R_g and R_H are approximately proportional to M_w, shown by the power law exponent of 1 indicated by the blue lines in Fig. 2 *A* and *B*, as expected for a rod morphology. The average value of $\rho \simeq 2$ is also compatible with that of polydisperse rods (30). A second scenario could be a bidisperse population of mostly tetramers and between 2% and 12% filaments. In this scenario, the different measured values for length and mass result from differences in the fraction of short filaments in the bidisperse system.

It should be noted that the situation before initiation of the assembly is likely due to aggregates of tetramers caused by impurities in the solution that can act as seeds. Those aggregates are probably not identical to the higher-order structures that we find as intermediate steps during vimentin assembly. Moreover, we have shown previously that the addition of KCl transfers the tetramers into an assembly-competent state and thus initiates the process (6, 31) and this transfer could be associated with a solubilization of individual tetramers.

Kinetics of Assembly. We select the least aggregated sample ($M_w \simeq 3.2 \times 10^5$ g/mol, $R_g \simeq 25$ nm; Table 1) to study the kinetics of vimentin assembly. The concentration of this sample is (0.07 ± 0.02) g/L. Assembly is induced upon addition of 0.1 M KCl at a volume ratio of 1:1. Given the low protein concentration, corrections to M_w and D_z arising from A_2 and k_D (~0.5–3%) are neglected. Fig. 3 shows a plot of M_w, R_g, R_H, and ρ as a function of time, where $t = 0$ corresponds to the mixing time point. The values before the addition of salt ($t = 0$) are indicated as large symbols at $t = 0.03$ min. The first readings correspond to $t \simeq 0.3$–0.5 min after mixing. Clear changes in the state of vimentin are apparent already at the earliest measured time points. Within the first 0.3 min, the molecular weight increases to a value of 10^6 g/mol, whereas R_g remains constant within experimental error and R_H increases by 20%. Further, for $t \leq 10$ min, M_w continues to increase by a factor of 1.5 whereas R_H grows only slightly and

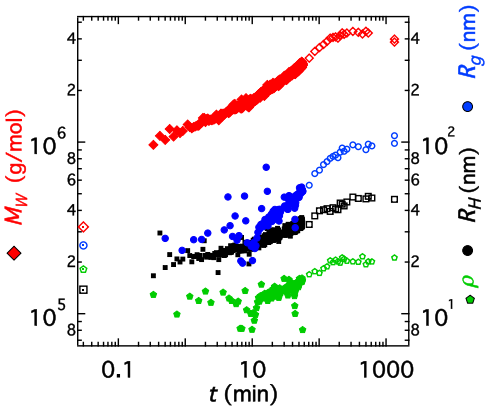

Fig. 3. Vimentin assembly kinetics. M_w (red diamonds), R_g (blue circles), R_H (black squares), and ρ (green diamonds) are plotted against time for a vimentin solution (0.07 g/L protein, 0.05 M KCl). Symbols at $t = 0.03$ min correspond to the values of vimentin before addition of KCl; i.e., $t = 0$. ρ is multiplied by a factor of 10.

R_g remains constant within a fairly large experimental uncertainty. For $t \geq 10$ min, we observe an increase of R_g and ρ.

If the trend in M_w in Fig. 3 is extrapolated to the point representing the initial state, two phases in the assembly process become apparent. Assuming rod-shaped assemblies, our data suggest that lateral assembly essentially takes place during the first minute. In the time range of 1 min $\leq t \leq 10$ min lateral aggregation appears to be completed whereas elongation starts to become noticeable, thus establishing transition from the first to the second phase. Thereafter the data indicate elongational growth and an increase in the aspect ratio of the assemblies. Due to the specific length and time scales probed by light scattering, the focus of this work is a quantitative analysis of the second phase. At $t \simeq 2$ h, M_w decreases. Given that the length of the assemblies at this time is of the order of several hundred nanometers ($R_g \simeq 100$ nm corresponds to lengths L of $\simeq 300$ nm), this is likely due to sedimentation. The polydispersity remains approximately constant at a value of 1.3 throughout the experiment.

The correlation between M_w and R_g, plotted in Fig. 4, gives insight into the morphology of the assembled structures: Rod-like morphologies yield $R_g \sim M_w$ whereas compact structures (e.g., spheres) lead to $R_g \sim M_w^{1/3}$. Lateral aggregation of rods with a high aspect ratio $L \gg d$ leads to $R_g \sim M_w^0 \sim$ const. For $t \leq 10$ min (circles with a cross in Fig. 4), the scatter in R_g is fairly large. However, the values scatter around 29 nm, which is only 15% higher than the value of 25 nm determined at $t = 0$ (Fig. 2), confirming that growth is dominated by lateral assembly in the beginning of the assembly process. Data for $10 \leq t \leq 60$ min are plotted as solid circles. Data for $t \geq 60$ min, obtained from 30 angle readings with acquisition times of 15 s per angle and therefore displaying significantly smaller errors, are plotted as open circles. These longer acquisition times were possible because the growth process became sufficiently slow at $t = 60$ min. A best fit to the data

Table 1. M_w, R_g, and R_H for samples before the addition of KCl and parameters from fits to the kinetic model at $c_S = 0.05$ M and varying c

	Samples in sodium phosphate buffer			Kinetic parameters				
C, g/L	M_w, g/mol	R_g, nm	R_H, nm	p	$\delta\omega$, rad·nm	k_n, M^{p-1}/s	M_L*, ×10^3 g/(mol·nm)	d_F, nm
0.09 ± 0.01	3.5×10^5	27	13	9 ± 1	0.34 ± 0.05	–	45	24
0.07 ± 0.02	3.2×10^5	25	14	6 ± 1	0.17 ± 0.02	2×10^{35}	29	34
0.06 ± 0.01	3.9×10^5	32	15	5 ± 1	0.14 ± 0.02	6×10^{29}	25	22

*M_L is the mass per unit length of the ULFs [$M_L = (60/43)pM_L^{tet}$].

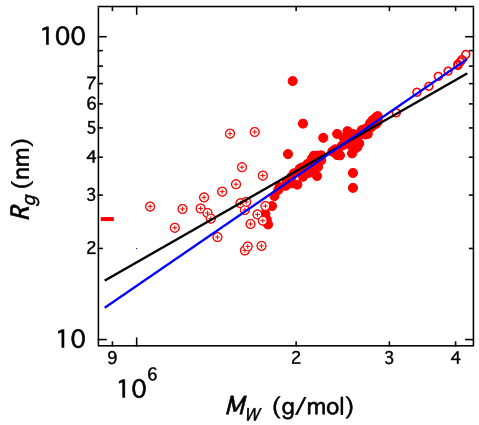

Fig. 4. Morphology of the emerging assemblies. R_g is plotted against M_w for the kinetic run shown in Fig. 3. Circles with a cross correspond to $t \leq 10$ min and solid circles to $10 \leq t \leq 60$ min. Open circles correspond to data for $t \geq 60$ min, which were obtained from 30 angle readings. The black line corresponds to polydisperse rods with $p.d. = 1.3$ and $M_L = 22 \times 10^3$ g/(mol·nm) (Eq. S4). The blue line corresponds to a best-fit power law. The red bar on the R_g axis corresponds to the R_g value before the aggregation process starts.

at $t \geq 10$ min with the rod model and $p.d. = 1.3$ and constant mass per unit length yields $M_L = 22 \times 10^3$ g/(mol·nm) ($\simeq 6$ times that of a tetramer). The best fit to a power law yields an exponent of 1.3. Rigid rods may yield an apparent exponent greater than 1 if either $p.d.$ increases or M_L decreases as assembly takes place. In the case of vimentin assembly, we expect $p.d.$ of the emerging filaments to increase due to assembly. As expected from previous work (3, 4), the exponent allows us to rule out growth via a monomer addition mechanism that would result in an exponent of $\simeq 0.5$ for rods (32).

Kinetic Model. Based on the above findings and on earlier work by Hermann et al. (4) we adopt a two-step model. In the first step, p tetramers assemble laterally to form ULFs with a rate constant k_n (schematic in Fig. 1*B*). This step does not significantly affect the radius of gyration R_g of the particles. The first step is modeled by a reaction of order p where p tetramers assemble laterally at once. We are fully aware that this oversimplifies the process; however, our dataset in this stage does not allow any further consideration. In a second step ULFs associate end to end (Fig. 1*C*). The reaction constant for this step is $k_{i,j}$ and depends on the lengths of the two aggregating species. $k_{1,1}$ corresponds to the assembly of two ULFs to yield a longitudinal ULF dimer, $k_{2,1} = k_{1,2}$ corresponds to the assembly of a longitudinal ULF dimer with a ULF, etc. In addition to the filament length, $k_{i,j}$ is a function of d_F, the cross-sectional hydrodynamic filament diameter, and $\delta\omega$, the product of the maximum distance and angle between the ends of two filaments required for assembly (18, 23, 33–35). Further parameters needed for the model are the tetramer mass $M_{tet} = 214 \times 10^3$ g/mol, the tetramer length $L_{tet} = 60$ nm, and the filament length $L_F = (60 + 43(n_L - 1))$ nm, where n_L is the longitudinal degree of association of a filament and 43 nm is the length contributed to the filament by a ULF. Kinetic equations for this scheme have been derived by Tomski and Murphy (18) and Pallitto and Murphy (23) and are compiled in *Supporting Information*, *Kinetic Equations* along with analytical solutions for the cases $k_{i,j} = 0$ (just lateral assembly) and $k_n = \infty$ (instantaneous lateral assembly). The solutions to the equations for arbitrary values of k_n and $k_{i,j}$ used for fitting our kinetic data are obtained numerically.

Fig. 5*A* shows M_w as a function of time for the same sample discussed in Figs. 3 and 4. The model correctly captures the experimental data with three free parameters: k_n, $\delta\omega$, and p, collected in Table 1. An additional parameter d_F is needed but its value affects the fit to the M_w only very weakly (see *Supporting Information*, *Kinetic Equations* for details of the calculation and parameter estimates). The data display a power law of $M_w \propto t^{0.38}$ at long times, close to the $M_w \propto t^{1/3}$ behavior expected for thin rods aggregating end to end (*Supporting Information*, *Kinetic Equations*). Fig. 5 *B* and *C* shows R_g and R_H as a function of time along with the corresponding theoretical trends based on the fit to the M_w data in Fig. 5*A*, further adjusted to fit the R_g and R_H data. Adjustment is carried out by selecting one of the best fits to M_w vs. t achieved with three neighboring values of p. All three fits equally well describe M_w vs. t but exhibit varying quality for R_g vs. t with only one of them showing satisfactory agreement (*Supporting Information*, *Multiplicity of Fits*). Further, d_F is adjusted to fit the R_H vs. t data. The model describes the time variation of R_g and R_H correctly.

We note that if only one quantity (M_w, R_g, or R_H) is fitted, considerable uncertainty in the parameter estimates is observed. For example, if we fit only M_w, setting p to any value between 5 and 7, correspondingly different values of k_n and $\delta\omega$ result in equally good fits to the data (see Fig. S5). It is only when R_g is considered additionally, that we can restrict the valid fits. The same is true if we fit only R_g : We are able to obtain multiple combinations for p, k_n, and $\delta\omega$ that fit the time dependence of R_g but deviate largely from the M_w values (*Supporting Information*, *Multiplicity of Fits*).

Whereas most previous studies (4, 34, 36) quantitatively captured the first, lateral assembly step, the present work complements these results by focusing on the second, elongational assembly step.

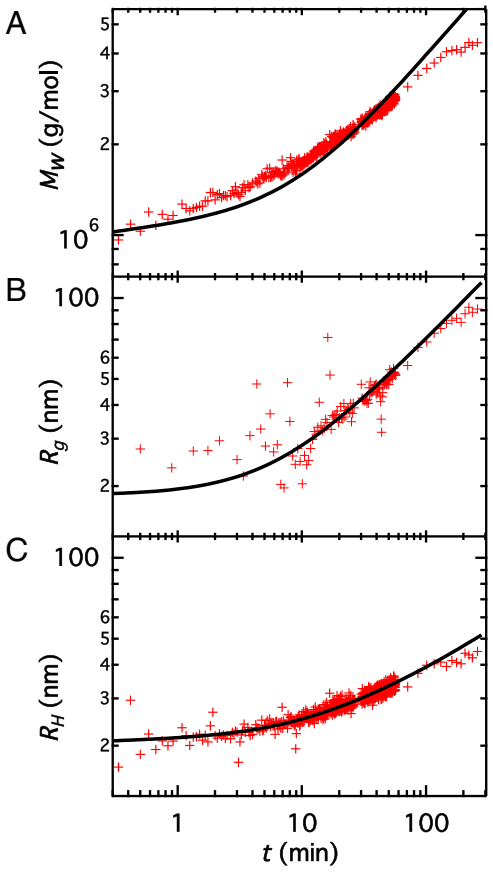

Fig. 5. (*A*) M_w against time for a 0.07-g/L vimentin solution in the presence of 0.05 M KCl. (*B*) R_g against time. (*C*) R_H against time. The black lines show the model fit for the reaction scheme outlined in Fig. 1. The equations used to calculate M_w, R_g, and R_H from this model are explained in *Supporting Information*, *Kinetic Equations*.

Just like SAXS (5), DLS and SLS are solution techniques, minimizing the influence of filament–substrate interactions, and do not require labeling or staining. Direct comparison of kinetic values with previously published results is difficult due to differences in temperature, protein, and salt concentration. However, the trends reported here are in qualitative agreement with previous results, i.e., lateral assembly within seconds (our fit suggests that 70–80% of the tetramers are consumed by the time of the first measurements) and elongation within $\sim 10^3$ s. The work of Portet (34) may be compared in more detail to our work: The mean filament length of a 0.1-g/L sample in 0.1 M KCl 20 min after dilution is ∼450 nm. Our values of $R_g \simeq 40-70$ nm translate into 100–200 nm contour length. The values of $\delta\omega$ ($\sqrt{8\tilde{p}}$ in model I of ref. 34) are in the range of 1–4 nm rad, an order of magnitude larger than ours. This faster growth is expected because the salt concentration and temperature are greater than for our samples.

Two additional samples with similar protein concentrations of $c = 0.06 \pm 0.01$ and 0.09 ± 0.01 g/L (Table 1) were investigated for comparison. Fits to the kinetic model are presented in Fig. S7. Qualitatively, the assembly process remains the same, with a lateral assembly step followed by end-to-end growth (*Supporting Information*, *Variability with Concentration*). The scatter in the values of p, k_n, and $\delta\omega$ compiled in Table 1 demonstrates the level of uncertainty in our results, probably due to inaccuracies in concentration measurements at such low values. The resulting mass per unit length of the ULFs varies from 25 to 45×10^3 g/(mol·nm), corresponding to approximately five to nine tetramers per ULF. Lateral assembly is too fast for the 0.09 g/L sample to model step one. Noteworthy, the values of p and M_L are close to the values expected from direct imaging using, e.g., electron microscopy (4), where typically $p = 8$ and $M_L = 40 \times 10^3$ g/(mol·nm) were found. However, variations between 20×10^3 g/(mol·nm) and 65×10^3 g/(mol·nm) were observed, even within one filament when the "kick-start" assembly mode has been used by direct mixing of two solutions as in this study. These values correspond to p ranging between 4 and 13. By contrast, slow dialysis leads to homogeneous filaments (4). The values of $d_F \simeq 22$–34 nm resulting from the fit in Fig. 5*C* are on the same order as the hydrodynamic diameter of 16–18 nm found by Hohenadl et al. (37) for the related IF protein desmin.

Evaluation of the Kinetic Model. Our model provides a good fit to the data; however, several important approximations must be noted: (*i*) We have assumed all reactions to be irreversible, which is probably true to a great extent in the light of the very slow subunit exchange observed in vitro (38); (*ii*) lateral assembly (step one) is assumed to occur for only a single value of p, whereas in fact it is well known that vimentin filaments exhibit heterogeneous M_L values (4, 39) when assembly is started by mixing of the solutions; (*iii*) the mean value of L is used to calculate the reaction constant for step two, which avoids having to solve a large number of differential equations; (*iv*) we use an approximate expression for the diffusion coefficients of rods, which may suffer at low aspect ratios; and (*v*) we use one of many possible assumptions for the initial state of our system. Given these considerations, the fit parameters collected in Table 1 must be taken as indicative values. Whereas agreement between data and model is good in general, the model predicts a slightly steeper increase of M_w with time. Following Hill (33), our model assumes the probability that a collision between two rods of lengths L_i and L_j results in aggregation varies as $p_{i,j} \propto 1/(L_i + L_j)^2$. As noted by Hill, he did not consider rotational motion or intermolecular excluded volume of rods (33). Thus, it seems reasonable that the length dependence of $p_{i,j}$ would deviate from his prediction. In fact, treating the exponent of $p_{i,j} \propto 1/(L_i + L_j)^{\alpha}$ as a free parameter yields a better fit to M_W with $\alpha \simeq 3.5$ (Fig. S6). This aspect is further discussed in *Supporting Information*, *Justification of Number of Free Parameters and Alternative Fit*.

Conclusions

We investigate the assembly of vimentin IF proteins into filaments in their native state, i.e., without labeling, staining, or adsorption to substrates. In situ observation of the assembly process is enabled by using multiangle, time-resolved SLS and DLS. Our kinetic model describes the two stages of the protein association: Lateral assembly of the rod-shaped subunits dominates growth for the first minute and end-to-end assembly of the emerging ULFs dominates for times longer than 10 min. Our datasets reveal average numbers of five to nine tetramers per cross-section, which is in agreement with previous results.

Materials and Methods

Preparation and Purification of Vimentin Protein. Human vimentin protein was recombinantly expressed in *Escherichia coli* and was purified after initial expression from inclusion bodies as described elsewhere (40). The quality of the protein was determined by SDS polyacrylamide gel electrophoresis (SDS/PAGE). Vimentin was stored at −80 °C in 8 M urea, 5 mM Tris-hydrochloric acid (Tris·HCl) (pH 7.5), 1 mM EDTA, 0.1 mM ethylene glycol tetraacetic acid (EGTA), 1 mM DTT, and 10 mM methyl ammonium chloride (MAC). Before the experiments, vimentin was renatured into tetramers by stepwise dialysis against 2 mM phosphate buffer (PB), pH 7.5, containing 8 M, 4 M, 2 M, and 1 M urea at room temperature for 30 min each. Finally, overnight dialysis into 2 mM PB was performed at 4 °C. All dialysis steps are performed using membranes of 50-kDa cutoff (Spectra/Por7; Spectrum Europe B.V.). For each dataset presented here, the protein concentration was determined by measuring the absorption at 280 nm with UV/visible (UV/Vis) spectroscopy (Nanodrop ND-1000; ThermoScientific Technologies). The concentration of several (≃ 20) samples was measured before and after filtering to check for possible absorption of protein by the filter but no such effect was found.

Light-Scattering Experiments. Kinetic SLS and DLS experiments were carried out on an ALV CGS-3 Compact Goniometer System equipped with eight detectors, spaced 8° from each other. A He-Ne laser from Soliton with $\lambda = 632.8$ nm was used as the light source. The full accessible q range with this instrument is $0.0046 \le q \le 0.024$ nm^{-1}. For a typical kinetic reading, the starting angle was fixed at 25°, resulting in a q range of $0.0046 \le q \le 0.017$ nm^{-1}. Further details on the instrument can be found in ref. 27. Cylindrical quartz cuvettes of 20 mm diameter, washed with freshly distilled acetone, were used as scattering cells. To study the kinetics of assembly, 3 mL of vimentin solution was filtered into a cuvette, followed by 3 mL of the KCl solution. The cuvette was shaken to promote mixing and placed into the light-scattering instrument and the measurement started. The times from mixing to the first reading are typically 15–30 s. All filters (0.22 μm cellulose ester) were washed with the corresponding solvent before use. A second combined SLS/DLS (ALV-CGS 5000E) instrument with two detectors at a single angle was used for samples that were not time dependent (before the addition of salt) or for measurements with slow kinetics such that no significant change occurred in the typical acquisition time for a scattering curve (≃ 5 min).

Data Analysis. Light-scattering data were reduced using standard procedures. The solvent intensity was subtracted from that of the sample. Absolute calibration was performed against toluene. For kinetic readings, where only eight angles are available, R_g, M_w, D_z, and C were obtained from linear regression of Eqs. **1** and **2**, setting A_2 and $k_D = 0$ (see Fig. S3). Readings affected by the presence of dust are omitted (see Fig. S4). M_w/M_n was obtained from least-squares fitting of Eqs. **S8** and **S9** (*Supporting Information*, *Application of the Rod Model to Light Scattering*). $dn/dc = 0.186$ cm^3/g (41) was assumed for all samples. For full angular readings, where a wide q range is available, SLS data were fitted either using the above procedure or using a polydisperse form factor as described in *Supporting Information*, *Application of the Rod Model to Light Scattering* (see Fig. S1). Fitting of the kinetic data was performed numerically, using the Runge–Kutta method, implemented in Igor Pro v6.36. A detailed description of the fitting procedure is provided in *Supporting Information*, *Kinetic Equations*.

ACKNOWLEDGMENTS. We thank Harald Herrmann for fruitful discussions, Susanne Bauch for technical assistance, and Sanjib Saha for assistance with the SLS/DLS measurements. This work was supported by the German Research Foundation (DFG) in the framework of SFB 755 "Nanoscale Photonic Imaging," project B07 and DFG KO 3572/5-1, as well as the Helmholtz Gemeinschaft in the framework of the Virtual Institute VH-VI-403 "In-Situ Nano-Imaging of Biological and Chemical Processes."

1. Fletcher DA, Mullins RD (2010) Cell mechanics and the cytoskeleton. *Nature* 463(7280):485–492.
2. Omary MB, Ku NO, Strnad P, Hanada S (2009) Toward unraveling the complexity of simple epithelial keratins in human disease. *J Clin Invest* 119(7):1794–1805.
3. Herrmann H, Aebi U (1998) Intermediate filament assembly: Fibrillogenesis is driven by decisive dimer-dimer interactions. *Curr Opin Struct Biol* 8(2):177–185.
4. Herrmann H, et al. (1996) Structure and assembly properties of the intermediate filament protein vimentin: The role of its head, rod and tail domains. *J Mol Biol* 264(5):933–953.
5. Brennich ME, et al. (2011) Dynamics of intermediate filament assembly followed in micro-flow by small angle X-ray scattering. *Lab Chip* 11(4):708–716.
6. Brennich ME, et al. (2014) Impact of ion valency on the assembly of vimentin studied by quantitative small angle X-ray scattering. *Soft Matter* 10(12):2059–2068.
7. Hémonnot CYJ, Mauermann M, Herrmann H, Köster S (2015) Assembly of simple epithelial keratin filaments: Deciphering the ion dependence in filament organization. *Biomacromolecules* 16(10):3313–3321.
8. Strelkov SV, Schumacher J, Burkhard P, Aebi U, Herrmann H (2004) Crystal structure of the human lamin A coil 2B dimer: Implications for the head-to-tail association of nuclear lamins. *J Mol Biol* 343(4):1067–1080.
9. Kapinos LE, et al. (2010) Characterization of the head-to-tail overlap complexes formed by human lamin A, B1 and B2 "half-minilamin" dimers. *J Mol Biol* 396(3):719–731.
10. Meier M, et al. (2009) Vimentin coil 1aa molecular switch involved in the initiation of filament elongation. *J Mol Biol* 390(2):245–261.
11. Sokolova AV, et al. (2006) Monitoring intermediate filament assembly by small-angle x-ray scattering reveals the molecular architecture of assembly intermediates. *Proc Natl Acad Sci USA* 103(44):16206–16211.
12. Winheim S, et al. (2011) Deconstructing the late phase of vimentin assembly by total internal reflection fluorescence microscopy (TIRFM). *PLoS One* 6(4):e19202.
13. Nöding B, Köster S (2012) Intermediate filaments in small configuration spaces. *Phys Rev Lett* 108(8):088101.
14. Selser J (1979) A determination of polymer number-averaged and weight-averaged molecular weight using photon correlation spectroscopy. *Macromolecules* 12(5):909–916.
15. Hassan PA, Kulshreshtha SK (2006) Modification to the cumulant analysis of polydispersity in quasielastic light scattering data. *J Colloid Interface Sci* 300(2):744–748.
16. Holthoff H, Egelhaaf SU, Borkovec M, Schurtenberger P, Sticher H (1996) Coagulation rate measurements of colloidal particles by simultaneous static and dynamic light scattering. *Langmuir* 12(23):5541–5549.
17. Jouault N, Moulin E, Giuseppone N, Buhler E (2015) Light scattering strategy for the investigation of time-evolving heterogeneous supramolecular self-assemblies. *Phys Rev Lett* 115(8):085501.
18. Tomski SJ, Murphy RM (1992) Kinetics of aggregation of synthetic β-amyloid peptide. *Arch Biochem Biophys* 294(2):630–638.
19. Lomakin A, Teplow DB, Kirschner DA, Benedek GB (1997) Kinetic theory of fibrillogenesis of amyloid β-protein. *Proc Natl Acad Sci USA* 94(15):7942–7947.
20. Lomakin A, Chung DS, Benedek GB, Kirschner DA, Teplow DB (1996) On the nucleation and growth of amyloid beta-protein fibrils: Detection of nuclei and quantitation of rate constants. *Proc Natl Acad Sci USA* 93(3):1125–1129.
21. Walsh DM, et al. (1999) Amyloid β-protein fibrillogenesis. Structure and biological activity of protofibrillar intermediates. *J Biol Chem* 274(36):25945–25952.
22. Kusumoto Y, Lomakin A, Teplow DB, Benedek GB (1998) Temperature dependence of amyloid β-protein fibrillization. *Proc Natl Acad Sci USA* 95(21):12277–12282.
23. Pallitto MM, Murphy RM (2001) A mathematical model of the kinetics of β-amyloid fibril growth from the denatured state. *Biophys J* 81(3):1805–1822.
24. Yamakawa H (1971) *Modern Theory of Polymer Solutions* (Harper & Row Publishers, Inc, New York).
25. Yoshizaki T, Yamakawa H (1980) Dynamics of spheroid-cylindrical molecules in dilute solution. *J Chem Phys* 72(1):57–69.
26. Tirado MM, de la Torre JG (1980) Rotational dynamics of rigid, symmetric top macromolecules. Application to circular cylinders. *J Chem Phys* 73(4):1986–1993.
27. Michels R, Sinemus T, Hoffmann J, Brutschy B, Huber K (2013) Co-aggregation of two anionic azo dyestuffs at a well-defined stoichiometry. *J Phys Chem B* 117(28):8611–8619.
28. Cravillon J, et al. (2011) Controlling zeolitic imidazolate framework nano-and microcrystal formation: Insight into crystal growth by time-resolved in situ static light scattering. *Chem Mater* 23(8):2130–2141.
29. Burchard W (1983) Static and dynamic light scattering from branched polymers and biopolymers. *Adv Polym Sci* 48:1–124.
30. Schmidt M (1984) Combined integrated and dynamic light scattering by poly (γ-benzyl glutamate) in a helocogenic solvent. *Macromolecules* 17(4):553–560.
31. Saldanha O, Brennich ME, Burghammer M, Herrmann H, Köster S (2016) The filament forming reactions of vimentin tetramers studied in a serial-inlet microflow device by small angle x-ray scattering. *Biomicrofluidics* 10(2):024108.
32. Liu J, Rieger J, Huber K (2008) Analysis of the nucleation and growth of amorphous CaCO3 by means of time-resolved static light scattering. *Langmuir* 24(15):8262–8271.
33. Hill TL (1983) Length dependence of rate constants for end-to-end association and dissociation of equilibrium linear aggregates. *Biophys J* 44(2):285–288.
34. Portet S (2013) Dynamics of in vitro intermediate filament length distributions. *J Theor Biol* 332:20–29.
35. Portet S, et al. (2009) Vimentin intermediate filament formation: In vitro measurement and mathematical modeling of the filament length distribution during assembly. *Langmuir* 25(15):8817–8823.
36. Kirmse R, et al. (2007) A quantitative kinetic model for the in vitro assembly of intermediate filaments from tetrameric vimentin. *J Biol Chem* 282(25):18563–18572.
37. Hohenadl M, Storz T, Kirpal H, Kroy K, Merkel R (1999) Desmin filaments studied by quasi-elastic light scattering. *Biophys J* 77(4):2199–2209.
38. Nöding B, Herrmann H, Köster S (2014) Direct observation of subunit exchange along mature vimentin intermediate filaments. *Biophys J* 107(12):2923–2931.
39. Herrmann H, Aebi U (1999) Intermediate filament assembly: Temperature sensitivity and polymorphism. *Cell Mol Life Sci* 55(11):1416–1431.
40. Herrmann H, Kreplak L, Aebi U (2004) Isolation, characterization, and in vitro assembly of intermediate filaments in intermediate filament cytoskeleton. *Methods Cell Biol* 78:3–24.
41. Zhao H, Brown PH, Schuck P (2011) On the distribution of protein refractive index increments. *Biophys J* 100(9):2309–2317.